Computational and Structural Biotechnology Journal 19 (2021) 3978–3989

COMPUTATIONAL AND STRUCTURAL BIOTECHNOLOGY JOURNAL

journal homepage: www.elsevier.com/locate/csbj

Insights into the molecular mechanism of positive cooperativity between partial agonist MK-8666 and full allosteric agonist AP8 of hGPR40 by Gaussian accelerated molecular dynamics (GaMD) simulations

Xiaoli An [a], Qifeng Bai [b], Zhitong Bing [c], Huanxiang Liu [d,*], Xiaojun Yao [a,e,*]

[a] State Key Laboratory of Applied Organic Chemistry and Department of Chemistry, Lanzhou University, Lanzhou 730000, China
[b] School of Basic Medical Science, Lanzhou University, Lanzhou, China
[c] Institute of Modern Physics of Chinese Academy of Sciences, Gansu Province, Lanzhou, China
[d] School of Pharmacy, Lanzhou University, Lanzhou 730000, China
[e] State Key Laboratory of Quality Research in Chinese Medicine, Macau Institute for Applied Research in Medicine and Health, Macau University of Science and Technology, Taipa, Macau, China

ARTICLE INFO

Article history:
Received 31 March 2021
Received in revised form 7 July 2021
Accepted 8 July 2021
Available online 10 July 2021

Keywords:
hGPR40
Positive binding cooperativity
Partial agonist
AgoPAM
Gaussian accelerated molecular dynamics simulation

ABSTRACT

Activation of human free fatty acid receptor 1 (FFAR1, also called hGPR40) enhances insulin secretion in a glucose-dependent manner. Hence, the development of selective agonist targeting hGPR40 has been proposed as a therapeutic strategy of type 2 diabetes mellitus. Some agonists targeting hGPR40 were reported. The radioligand-binding studies and the crystal structures reveal that there are multiple sites on GPR40, and there exists positive binding cooperativity between the partial agonist MK-8666 and full allosteric agonist (AgoPAM) AP8. In this work, we carried out long-time Gaussian accelerated molecular dynamics (GaMD) simulations on hGPR40 to shed light on the mechanism of the cooperativity between the two agonists at different sites. Our results reveal that the induced-fit conformational coupling is bidirectional between the two sites. The movements and rotations of TM3, TM4, TM5 and TM6 due to their inherent flexibility are crucial in coupling the conformational changes of the two agonists binding sites. These helices adopt similar conformational states upon alternative ligand or both ligands binding. The Leu138$^{4.57}$, Leu186$^{5.42}$ and Leu190$^{5.46}$ play roles in coordinating the rearrangements of residues in the two pockets, which makes the movements of residues in the two sites like gear movements. These results provide detailed information at the atomic level about the conformational coupling between different sites of GPR40, and also provide the structural information for further design of new agonists of GPR40. In addition, these results suggest that it is necessary by considering the effect of other site bound in structure-based ligands discovery.

1. Introduction

The free fatty acid receptor 1 (FFAR1, also called GPR40) is a member of the class A G protein-coupled receptors (GPCRs). The GPR40 is highly expressed in pancreatic β cells [1,2], and has been identified as a receptor for medium and long-chain saturated and unsaturated FFAs [1,3,4]. Activation of GPR40 enhances glucose-stimulated insulin secretion [1,5–7]. Hence, the human GPR40 (hGPR40) has been proposed as a therapeutic target of type 2 diabetes mellitus [1,8–10]. And GPR40 agonists for the treatment of type 2 diabetes mellitus offer advantages with inducing insulin secretion in a glucose-dependent manner without inducing hypoglycemia [8,9]. A range of synthetic agonists of GPR40 has been reported [11–20], the most representative TAK-875 in the treatment of type 2 diabetics mellitus proceeded into phase III clinical trials [11,21,22]. Nevertheless, TAK-875 development was terminated because of potential liver toxicity [23]. Moreover, a later study indicated that TAK-875 inhibits hepatobiliary transporters, which provides potential mechanisms for TAK-875 induced liver injury [24]. Accordingly, this also puts forward requirement to discover or design a selective agonist of GPR40.

* Corresponding authors State Key Laboratory of Applied Organic Chemistry and Department of Chemistry, Lanzhou University, Lanzhou 730000, China (X. Yao).
E-mail addresses: hxliu@lzu.edu.cn (H. Liu), xjyao@lzu.edu.cn (X. Yao).

https://doi.org/10.1016/j.csbj.2021.07.008
2001-0370/

Radioligand-binding interaction studies demonstrate that the presence of multiple ligand-binding sites on GPR40 [25], and there exist positive heterotropic cooperativity and positive functional cooperativity between the full allosteric agonists (AgoPAMs) and partial agonists. The crystal structures of GPR40 respectively bound with partial agonist TAK-875 [26], with partial agonist MK-8666, with MK-8666 and AgoPAM AP8 [27] were reported. These crystal structures reveal two distinct sites, the partial agonists TAK-875 and MK-8666 bind at the site that engages between transmembrane helices 3–5 (TM3-5) and the extracellular loop 2 (ECL2) regions; the AgoPAM AP8 sits outside the transmembrane helical bundle, a pocket formed by TM3, TM4, TM5 and intracellular loop 2 (ICL2) (Fig. 1). Simultaneously, the structural comparison reveals an induced-fit conformational coupling between the partial agonist and AgoPAM binding sites [27]. The rearrangements of the TM4 and TM5 and transition of the ICL2 into a short helix likely involve the positive binding cooperativity between the partial agonist and the AgoPAM [27]. However, static crystal structures in specific experimental conditions limit the conformations exploration of receptors upon binding various ligands. We have less knowledge of the positive binding cooperativity between these ligands from the crystal structures.

The molecular dynamics (MD) simulations provide dynamical properties of the interaction between ligands and receptors and conformational dynamics of biomolecules at atomic level. While, the insufficient sampling of conventional MD (cMD) due to the large energy barrier between various intermediates limits the study of large biomolecular systems. The enhanced sampling methods [28–33], by adding boost potential on a system or a set of predefined reaction coordinates, enable the biomolecular systems to overcome high energy barriers in the free energy landscape and sample in multiple conformational state spaces. The Gaussian accelerated molecular dynamics (GaMD) [29] simulations allow exploring the biomolecular conformational space without the need to set predefined reaction coordinates and achieves unconstrained enhanced sampling. The GaMD has been proved to be a powerful enhanced sampling method in the study of large proteins such as GPCRs [34–40].

Herein, we performed a total of 16 μs GaMD simulations on GPR40 to shed light on the mechanism of positive binding cooperativity between the partial agonist MK-8666 and AgoPAM AP8. We compared the conformational dynamics of GPR40 respectively bound to MK-8666, AP8, both MK-8666 and AP8, and apo state. Moreover, we estimated the binding affinity of MK-8666 and AP8 in absence and presence of another ligand by Molecular Mechanics/Generalized Born Surface Area (MM/GBSA) [41]. We re-docked AP8 to dominant structures extracted from GaMD simulations and crystal structures of GPR40, and calculated the RMSDs of redocked poses of AP8 by referencing the natural binding pose of AP8 in crystal structure. These results reveal a bidirectional induced-fit conformational coupling between the partial agonist and AgoPAM binding sites. And the positive cooperativity between the MK-8666 and AP8 is bidirectional. The rotations and shifts of TM3, TM4, TM5 and TM6 play critical roles in coupling the two sites. Upon alternative ligand bound of the two sites, the conformation changes of the other site by rearrangements of these helices. The movements of these residues are coordinated like gear movements. Besides, our results could be used in structure-based ligands discovery or structure-guided optimization of ligands by considering other modulators binding, and also could be used in combined drugs in drug therapy.

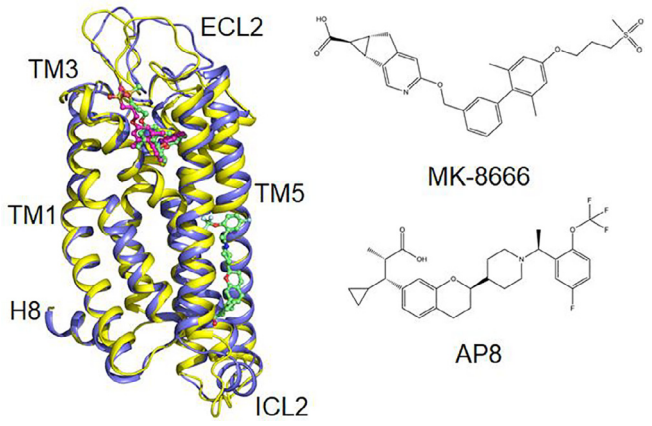

Fig. 1. The crystal structures of GPR40 in binary complex (yellow) with MK-8666 (represented by stick, magenta) and in ternary complex (purple) with MK-8666 and AP8 (represented by stick, green). (For interpretation of the references to color in this figure legend, the reader is referred to the web version of this article.)

2. Simulation methods

2.1. The simulation systems

For the purpose of investigating the positive binding cooperativity between the partial agonist and AgoPAM, the crystal structures of GPR40 in a binary complex with MK-8666 and in a ternary complex with MK-8666 and AP8 were used as start points (Fig. 1). The crystal structures were obtained from the PDB database (PDB code: 5TZR, 5TZY; resolution: 2.20 Å, 3.22 Å) [27]. The T4 lysozyme (T4L) fusion protein and solvate molecules of the crystal construct were deleted except water molecules. The mutational residues were mutated back. The missing residues of ICL2 (Leu112-Arg119) of the binary complex were built by the protein preparation wizard of Schrödinger 2015 [42]. The missing residues of ICL3 (Arg211-His216) were built by referencing the refined structure of the ternary complex deposited in GPCRdb [43]. The helix 8 (H8) was built by referencing the crystal structure of human protease-activated receptor-2 (PAR2) (PDB code: 5NDD) [44], the root mean square deviation (RMSD) is 0.38 Å by aligning the TM7 of GPR40 and PAR2 (the RMSD is 1.82 Å of 158 CA atoms by aligning the two structures). Finally, we prepared four systems denoted as GPR40-apo (MK-8666 was removed from binary complex), binary complex GPR40-MK6 (abbreviated binary complex of GPR40 and MK-8666), binary complex GPR40-AP8 (MK-8666 was removed from ternary complex) and ternary complex GPR40-MK6-AP8.

The membrane around the transmembrane domain (TMD) of GPR40 was built by 85 Å ×85 Å 1-palmitoyl-2-oleoylsn-*glycero*-3-phosphocholine (POPC) bilayers using CHARMM-GUI web server [45–47], the receptor crystal structure pre-aligned in the OPM (Orientations of Proteins in Membranes) database [48]. Each system was solvated by 10 Å with a truncated rectangular box of TIP3P waters [49] and neutralized with a concentration of 0.15 M NaCl.

The proteins were modeled using the AMBER FF14SB force field [50], the ligands were modeled using the generalized AMBER force field (GAFF) [51], and the LIPID11 force filed [52] was utilized for POPC. Geometry optimization and the electrostatic potential calculations on the ligands were performed at the HF/6-31G* level in the Gaussian09 software [53], and the partial charges were calculated with the RESP [54]. The force field parameters for the ligands were created by the Antechamber package.

2.2. The equilibration conformations

The energy minimization and equilibration were conducted by AMBER16 in order to equilibrate the systems. Firstly, to remove

bad contacts in the initial structures, the steepest descent and the conjugate gradient methods were carried out. After energy minimization, each system was gradually heated in NVT ensemble from 0 to 300 K in 300 ps. Subsequently, constant temperature equilibration at 300 K for a total of 3 ns was performed to adjust the solvent density in NPT ensemble with periodic boundary conditions; an integration step of 2 fs was used. The particle mesh Ewald (PME) algorithm [55] was employed to treat long-range electrostatic interactions, while the non-bonded interactions were calculated based on a cutoff of 10 Å. The SHAKE algorithm [56] was applied to constrain all covalent bonds involving hydrogen atoms.

2.3. Gaussian accelerated molecular dynamics (GaMD) simulations

The GaMD imposes a harmonic boost potential to smoothen the biomolecule system potential energy surface, which enables unconstrained enhanced sampling and free energy profiles obtained from reweighting of the GaMD simulations without the need to set predefined reaction coordinates. When the system potential (V) is less than the referenced energy (E), a harmonic boost potential (ΔV) is added. In the present study, the GaMD simulations of all the four systems were performed by Amber16 software and a GaMD patch. The final structures from the abovementioned equilibration procedure were used in the GaMD simulations. Initially, $\kappa_0 = 1.0$, $\sigma D = 6$, $\sigma V = 6$. The GaMD simulations included 10 ns short cMD simulation used to collect potential statistics (V_{max} and V_{min}) for calculating the GaMD acceleration parameters, 50 ns equilibration after adding the boost potential, and finally 4 μs dual-boost GaMD production produced with randomized initial atomic velocities for each system.

2.4. MM/GBSA binding energy

MM/GBSA was used to estimate the binding free energy of MK-8666 and AP8 interacting with GPR40. The final structures produced in GaMD simulations were used as the initial coordinates to perform cMD simulations. The RMSDs of backbone atoms of GPR40 are present in Fig. S3) for the 300 ns cMD trajectory. 500 snapshots were sampled evenly spaced from the last 50 ns of the cMD runs to estimate enthalpic contributions to binding of MK-8666 and AP8, respectively. Simultaneously, 50 snapshots were sampled evenly spaced from the last 50 ns of the cMD runs to estimate enthalpic and entropic contributions to binding of MK-8666 and AP8, respectively. Because of the almost identical values of enthalpic contributions calculated with 500 and 50 snapshots (Tables S1 and S2), we finally calculated the binding free energy by sampling 50 snapshots (Table 1). Per-residue energy decomposition was performed to evaluate the energy contribution of each residue.

3. Results and discussion

3.1. The effect of AgoPAM on partial agonist binding site and the binding stability of MK-8666

We carried out long-time GaMD simulation on each prepared system. And we intended to study the mechanism of positive binding cooperativity between the partial agonist MK-8666 and AgoPAM AP8 by analyzing the conformational dynamics of GPR40 and binding free energy of MK-8666 and AP8.

First, we monitored the root mean square deviations (RMSDs) of backbone atoms of GPR40 with reference to the corresponding crystal structures (PDBID: 5TZR and 5TZY) during the simulations (Fig. 2). Fig. 2A indicate that significant conformation changes take place in the early stage of simulations for each system, and all systems are convergent in the late simulations. Accordingly, we carried out hierarchical agglomerative clustering to cluster each trajectory into five clusters using RMSD of protein backbone as a metric (Fig. S4). And we superposed dominant structures that were extracted from the center of the first cluster with the largest population for each system (Fig. 2B). In the MK-8666 binding site, the interhelical space of extracellular ends of TM3 and TM4, as well as ECL2 make up the pocket entrance. The extracellular ends of TM3 and TM4 deflect toward TM2 in GPR40-apo compared to the other three systems, especially the TM4 presents significant flexibility in GPR40-apo (Fig. 2B and S5A). Accordingly, we measured the angle α formed by TM2 (center of mass of CA atoms of Pro40-Val43)-TM3 (center of mass of CA atoms of Tyr91-Gly94)-TM4 (center of mass of CA atoms of Val141-Leu144) to characterize deflection of extracellular end of TM4 (Fig. S6A).

Fig. 3A shows that angle α of GPR40-apo is significantly smaller than other systems during the simulation. The angles α of GPR40-MK6 and GPR40-AP8 increase in the early stage of simulations, and after that, steady fluctuate during the simulations. Furthermore, we extracted representative structures from each cluster of each system, and superposed the five representative structures respectively. Correspondingly, the extracellular ends of TM4 present various conformations in GPR40-MK6 and GPR40-apo (Fig. 3C and D). In comparison, the extracellular ends of TM4 are superposed well in GPR40-MK6-AP8 and GPR40-AP8 (Fig. 3E and F). The distinct conformational dynamics of TM4 among these systems indicate that AP8 binding stabilizes the extracellular end of TM4. The AP8 interacts directly with the intracellular side of TM4. It is more than likely that AP8 stabilizes the MK-8666 binding by stabilizing the TM4.

We monitored the RMSDs of MK-8666 by referencing the natural binding mode of GPR40-MK6 and GPR40-MK6-AP8, respectively. Before that, we centered the trajectory only on the protein by referencing the corresponding crystal structure for each system. Fig. 3B shows that the fluctuation of RMSD of MK-8666 in GPR40-MK6-AP8 is more stable than in GPR40-MK6 after about 0.8 μs

Table 1
The binding free energy of MK-8666 and AP8 interacting with GPR40.

	MK-8666		AP8	
	GPR40-MK6	GPR40-MK6-AP8	GPR40-AP8	GPR40-MK6-AP8
ΔE_{vdw}	−56.42 (1.94)	−62.11 (3.07)	−55.68 (3.05)	−58.51 (3.24)
ΔE_{ele}	−14.11 (4.80)	−17.99 (4.41)	−16.12 (3.33)	−16.56 (3.36)
ΔE_{GB}	31.60 (4.29)	33.87 (2.46)	25.23 (2.07)	25.79 (1.92)
ΔE_{SURF}	−6.89 (0.24)	−7.59 (0.21)	−7.65 (0.21)	−7.99 (0.20)
$\Delta H_{binding}$	−45.82 (2.57)	−53.82 (3.33)	−54.23 (3.50)	−57.27 (3.56)
$T\Delta S_{binding}$	−27.57 (4.27)	−28.37 (3.92)	−27.62 (4.30)	−28.41 (3.55)
$\Delta G_{binding}$	−18.25 (4.83)	−25.45 (4.55)	−26.61 (5.39)	−28.86 (5.36)

ΔE_{vdw}: Van der Waals energy; ΔE_{ele}: electrostatic energy; ΔE_{GB}: polar solvation energy; ΔE_{SURF}: nonpolar solvation energy; $\Delta H_{binding}$: enthalpic contributions; $T\Delta S_{binding}$: entropic contributions; $\Delta G_{binding}$: binding free energy.

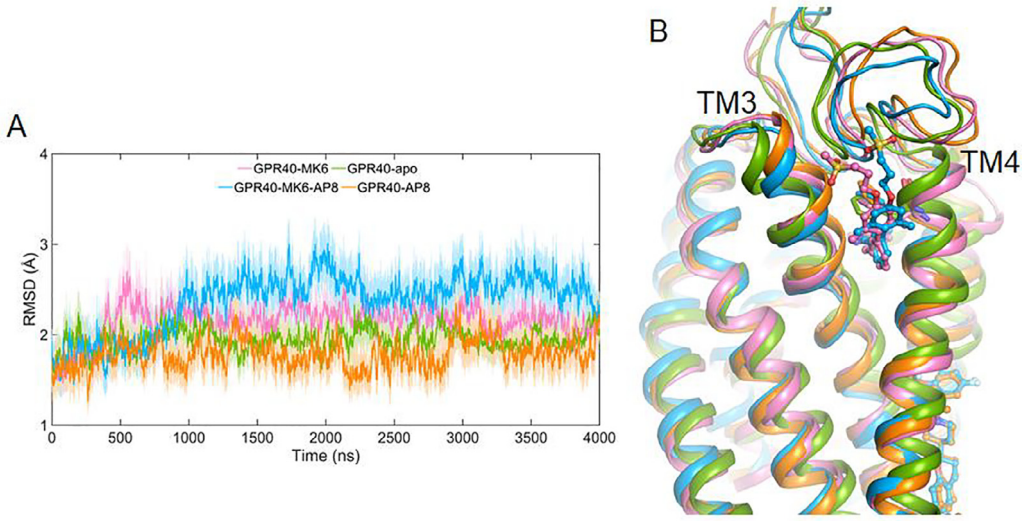

Fig. 2. A, The RMSDs of backbone atoms during the simulation. B, The representative structures extracted from clustering analysis (pink, GPR40-MK6; green, GPR40-apo; blue, GPR40-MK6-AP8; orange, GPR40-AP8). (For interpretation of the references to color in this figure legend, the reader is referred to the web version of this article.)

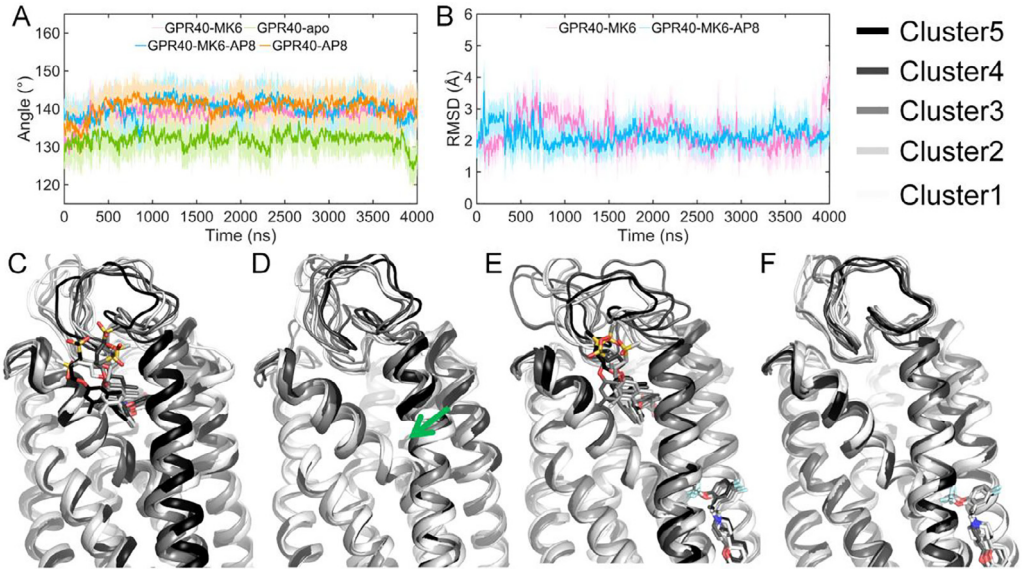

Fig. 3. A, Angle α evolves with time. B, The RMSD of non-hydrogen atoms of MK-8666. C-F, The representative structures extracted from each cluster by clustering analysis for GPR40-MK6, GPR40-apo, GPR40-MK6-AP8 and GPR40-AP8, respectively (the green arrow represent direction of movement of TM4). (For interpretation of the references to color in this figure legend, the reader is referred to the web version of this article.)

during the simulation. As shown in Fig. 3C and E, the binding mode of partial agonist MK-8666 is more diverse in GPR40-MK6 compared with GPR40-MK6-AP8. In particular, the part of the MK-8666 extending out of the helix bundle displays more diverse states. We noticed that hydrogen bonds formed between MK-8666 and backbone N atoms of Trp150 and Leu158 on ECL2 present almost throughout the simulations in GPR40-MK6-AP8 (Fig. 4A and B). The number of frames formed the hydrogen bonds accounted for 78.20% and 83.28% of the total frames, respectively. While the number of frames formed the hydrogen bonds accounted for 0.08% and 14.09% of the total frames respectively in GPR40-MK6. Therefore, the hydrogen bonds formed between MK-8666 and Trp150 and Leu158 on ECL2 are more stable in GPR40-MK6-AP8 compared with in GPR40-MK6 (Fig. 4). Furthermore, the binding free energy and per-residue energy decomposition analysis were carried out by MM/GBSA. As shown in Fig. 4C, Trp150 and Leu158 significantly contribute to the total binding energy in GPR40-MK6-AP8. Moreover, the electrostatic energy contributions of the two residues are significantly lower in GPR40-MK6-AP8 than in GPR40-MK6, which are the dominant component of energy contributions. Accordingly, the binding free energy of MK-8666 in GPR40-MK6 and GPR40-MK6-AP8 are −18.25 kcal/mol and −25.45 kcal/mol, respectively (Table 1). That is, AP8 bound simultaneously can increase the binding affinity of MK-8666. Hence, MK-8666 bound to GPR40 is more stable in GPR40-MK6-AP8. These stable hydrogen bonds contribute to stabilizing MK-8666 binding.

These results indicate that AP8 binding stabilizes the extracellular end of TM4. Therefore, the extracellular end of TM4 in GPR40-AP8 stays in a similar conformation as in MK-8666 bound GPR40.

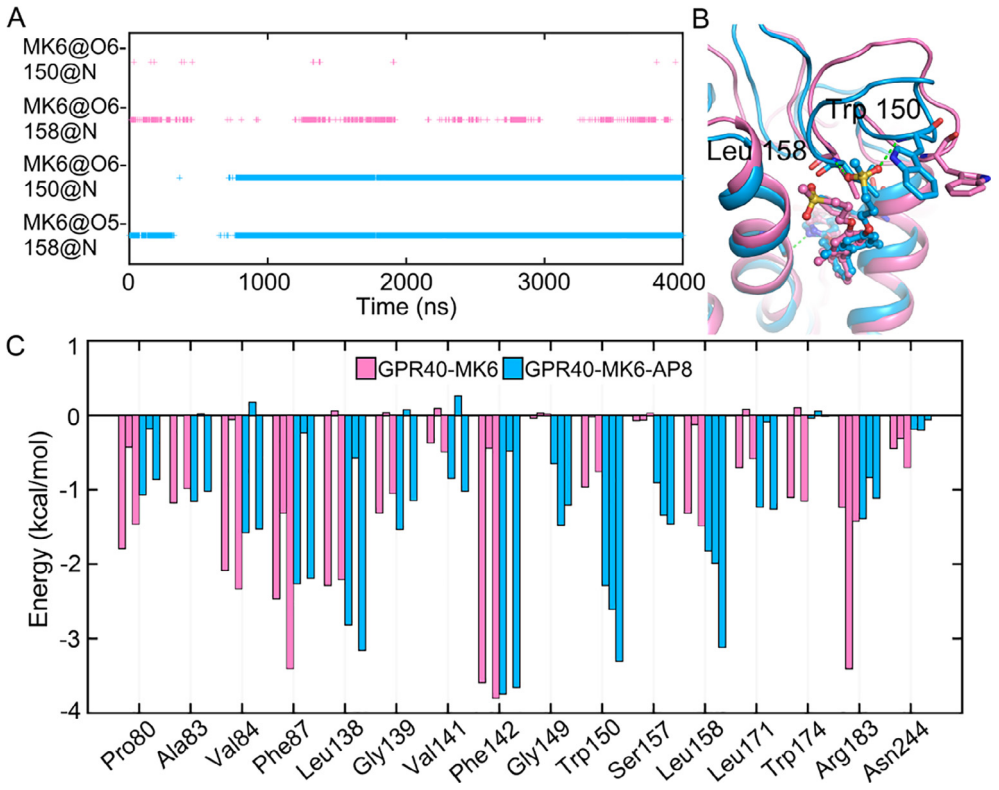

Fig. 4. A, The hydrogen bonds formed between backbone N atoms of Trp150 and Leu158 and MK-8666 evolves with time. B, The cartoon diagrams of MK-8666 interacting with ECL2 (pink: GPR40-MK6; blue: GPR40-MK6-AP8). C, The per-residue energy decomposition of GPR40-MK6 and GPR40-MK6-AP8, a group of same color represents Van der Waals energy, electrostatic energy and total energy contributions from left to right. (For interpretation of the references to color in this figure legend, the reader is referred to the web version of this article.)

Simultaneously, the stable extracellular end of TM4, as well as additional stable hydrogen bonds between the ECL2 and MK-8666 stabilize MK-8666 binding in GPR40-MK6-AP8.

3.2. The interhelical space entrance of MK-8666 binding site

The RMSF plot indicates that fluctuations of residues Phe87$^{3.33}$ and Phe88$^{3.34}$ are significant (Fig. S5). Therefore, we monitored the side chain dihedrals of the two residues (N-CA-CB-CG of Phe87, C-CA-CB-CG of Phe88), and obtained the probability mass function (PMF) of the two dihedrals. Fig. 5 shows the conformational spatial distribution of the two residues for each system. Obviously, the GPR40-MK6, GPR40-AP8 and GPR40-MK6-AP8 present almost identical conformational spatial distribution, except the GPR40-AP8, there is a minor energy basin (Fig. 5A, C and D). While GPR40-apo possesses a broad conformational spatial distribution in the two dimensions (Fig. 5B). We extracted the representative structures in the corresponding energy basins, the dominant conformational states of Phe87$^{3.33}$ and Phe88$^{3.34}$ in GPR40-MK6, GPR40-AP8 and GPR40-MK6-AP8 are similar (Fig. 5A, C and D).

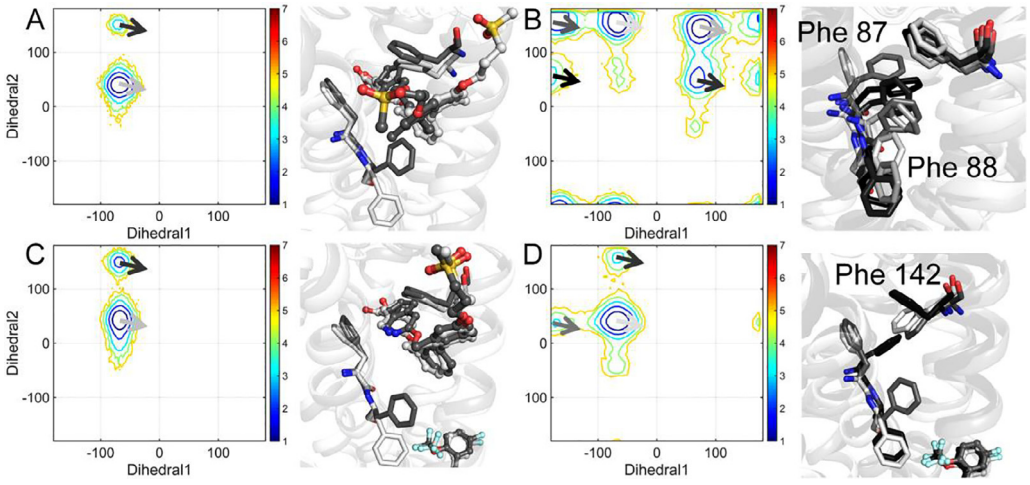

Fig. 5. The probability mass function (PMF) of side chain dihedral of Phe87 and Phe88. The representative structures extracted from energy basins are shown in right panel of PMF. A, GPR40-MK6; B, GPR40-apo; C, GPR40-MK6-AP8; D, GPR40-AP8.

The Phe87$^{3.33}$ stretches toward the inside of the helix bundle, Phe88$^{3.34}$ stretches down (toward the intracellular side). However, the conformational states of Phe87$^{3.33}$ and Phe88$^{3.34}$ in the GPR40-apo are various (Fig. 5B). The side chain of Phe87$^{3.33}$ deflects toward TM4, the side chain of Phe88$^{3.34}$ turns upward (toward the extracellular side) in dominant conformation. And in GPR40-apo, since the extracellular end of TM4 shifts toward TM3, the hydrophobic residues Phe87$^{3.33}$, Phe88$^{3.34}$ and Phe142$^{4.61}$ are close to each other. That makes the interhelical space between TM3 and TM4, the entrance of MK-8666, to be occluded (Fig. 5B and S7A). In GPR40-AP8, the pocket entrance in dominant conformation maintains the MK-8666 accessible state (Fig. 5D and S7B). Therefore, the binding of AP8 maintains interhelical space between TM3 and TM4 in a conformational state, where can bind MK-8666.

3.3. The conformational dynamics of MK-8666 binding pocket inside

We superposed and compared the dominant structures extracted from the center of the first cluster with the largest population for each system. At the bottom of the MK-8666 binding pocket in GPR40-apo, the extracellular end of TM6 shifts toward helix bundle, occupies the carboxylate binding subsite (Fig. 6A), and Tyr240$^{6.51}$ deflects toward TM2-TM3. In comparison, Tyr240$^{6.51}$ of GPR40-AP8 points toward the MK-8666 binding site, similar to the GPR40-MK6 and GPR40-MK6-AP8. In GPR40-AP8, extracellular end of TM6 slightly shifts toward helix bundle compared with GPR40-MK6 and GPR40-MK6-AP8, while that does not occupy carboxylate binding subsite compared with GPR40-apo. We measured the angle β formed by TM6 (centers of mass of CA atoms of Ser243-Ala246 and Cys236-Pro239) and TM3 (center of mass of CA atoms of Tyr91-Gly94) to characterize conformational dynamics of extracellular end of TM6 during the simulations (Fig. S6B). As shown in Fig. 6B, the angel β of GPR40-apo decreases at about 0.7 μs of simulation, and is significantly smaller than other systems. The dihedral of the side chain of Tyr240$^{6.51}$ (C-CA-CB-CG) in GPR40-apo increases significantly at about 2.8 μs and fluctuates stably in subsequent simulations (Fig. 6C). In comparison, the angle β in GPR40-AP8 is almost identical as in GPR40-MK6 and GPR40-MK6-AP8 throughout the simulations (Fig. 6C).

These results indicate that the presence of AgoPAM AP8 can stabilize the binding of MK-8666 in GPR40-MK6-AP8. Moreover, in GPR40-AP8, the presence of AP8 maintains the binding site of MK-8666 in a conformational state similar to that in GPR40-MK6-AP8 and GPR40-MK6. And we concluded from these results that the conformational difference between the GPR40-apo and GPR40-AP8 reveals an induced-fit conformational coupling between the AgoPAM AP8 and partial agonist binding site.

3.4. Effect of partial agonist on AgoPAM binding site

The AP8 binding pocket is a lipid-facing pocket formed by TM3, TM4, TM5 and ICL2 [27]. We compared the surface schematic diagrams of the pockets of dominant structures extracted from the center of the first cluster with the largest population (Fig. 7). In GPR40-MK6, the pocket maintains a similar topological structure as in AP8 bound GPR40 (Fig. 7A, C and D). But, in GPR40-apo, the top and bottom of the pocket are occupied (Fig. 7B). Furthermore, we redocked the AP8 to dominant structures for each system, as well as to the crystal structures by glide [57] of Schrödinger 2015. Furthermore, we calculated RMSDs of redocked poses of AP8 by referencing the natural binding pose of AP8 in the crystal structure. Fig. 8A displays the RMSDs of the best redocked binding poses of AP8 for each system. It can be seen that AP8 can be redocked into the pocket in binary complex GPR40-MK6 (RMSD = 1.51 Å), and superimposes well with the natural binding pose (Fig. 8B). While, AP8 can not be redocked into the pocket in binary crystal complex 5TZR (RMSD = 2.47 Å), the trifluoromethoxyphenyl and 2-methylpropanoic acid moieties of AP8 were excluded from the pocket (Fig. 8B).

Accordingly, we compared the detailed conformation changes of representative structures (Fig. 9). Fig. 9A shows that the TM4 shifts upward and twists, and the TM5 shifts downward and twists in GPR40-apo compared to other systems, which brings the Ile130$^{4.49}$, Leu189$^{5.45}$ and Leu190$^{5.46}$ to occupy the subsite of trifluoromethoxyphenyl moiety of AP8. At the bottom of the pocket, mainly due to the shifts of the intracellular tips of TM2 and TM4, which results in the subsite of 2-methylpropanoic acid to be occupied (Fig. 9A and B). The conformations of intracellular ends of TM2, TM3, TM4 and TM5 are similar in GPR40-MK6, GPR40-AP8 and GPR40-MK6-AP8. The results of redocking and conformational comparison indicate that the dominant conformation of GPR40-MK6 is more similar with GPR40-AP8 and GPR40-MK6-AP8.

In addition, we noted that the conformations of ICL2 are different between GPR40-MK6 and GPR40-apo in their dominant conformations (Fig. 9B). In GPR40-apo, ICL2 forms partial α-helical conformation (Fig. 9B and D); the Tyr114^{ICL2} points toward TM2, forming a hydrogen bond with Asn41$^{2.39}$ (Fig. 9B and S8B). Accordingly, the intracellular end of TM2 shifts toward TM4-TM5. However, the ICL2 in GPR40-MK6 is disordered (Fig. 9B and C), and the Tyr114^{ICL2} turns toward the outside of the helix bundle

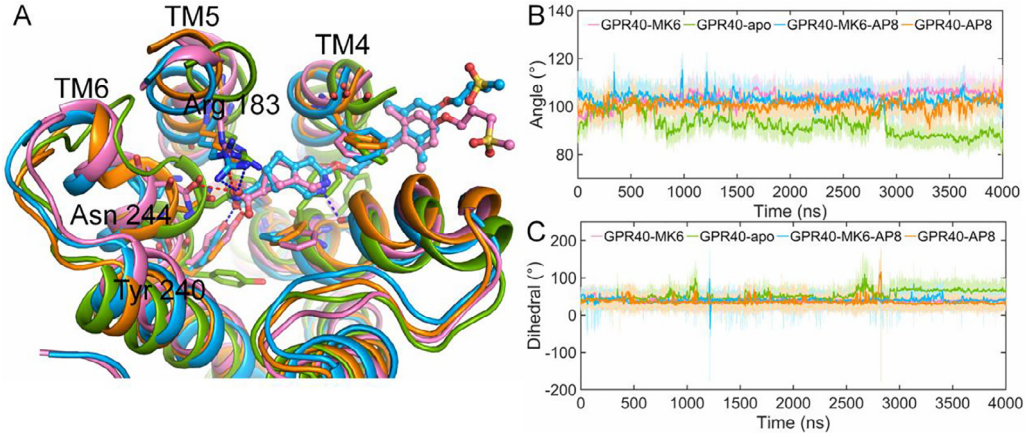

Fig. 6. A, The inside of MK-8666 binding pocket of representative structures extracted from clustering analysis. B, The angle β evolves with time. C, The side chain dihedral of Tyr240 evolves with time (GPR40-MK6: pink; GPR40-apo: green; GPR40-MK6-AP8: blue; GPR40-AP8: orange). (For interpretation of the references to color in this figure legend, the reader is referred to the web version of this article.)

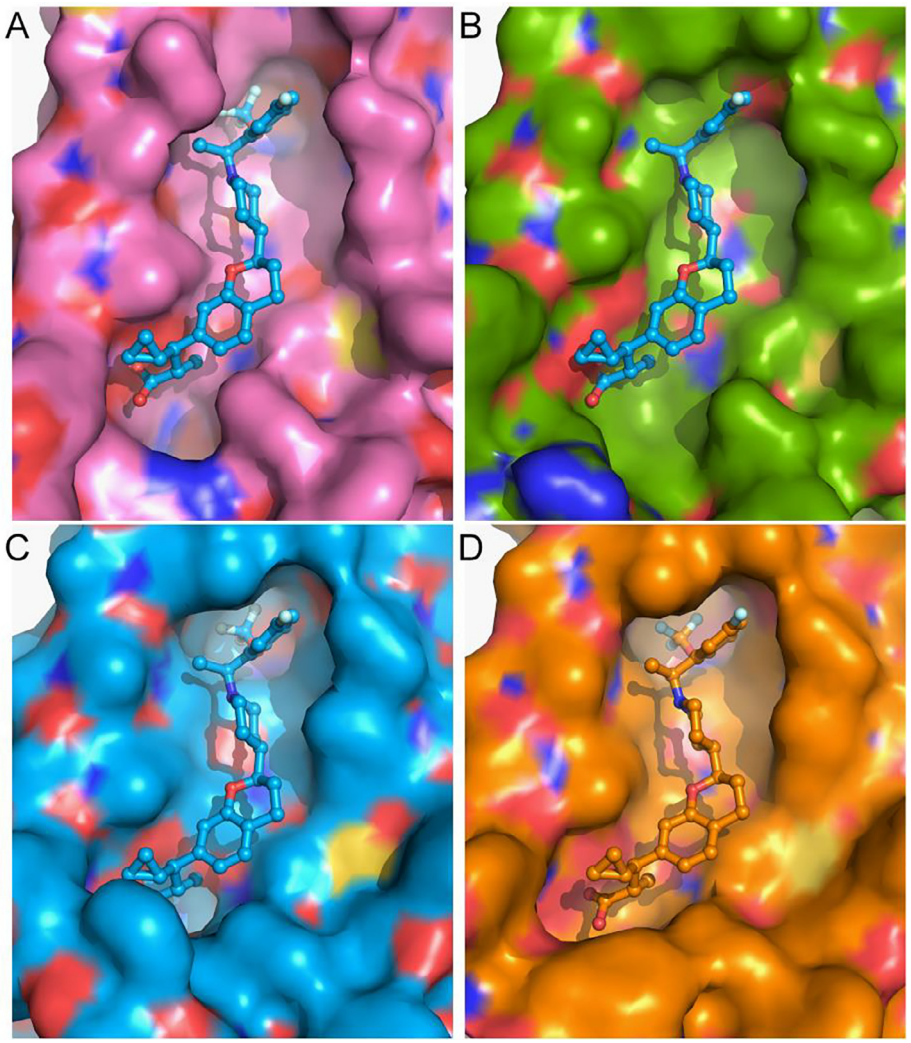

Fig. 7. The surface schematic diagrams of AP8 binding pocket (red is O atom, blue is N atom, gray is F atom, and the corresponding color described above is C atom). A, GPR40-MK6; B, GPR40-apo; C, GPR40-MK6-AP8; D, GPR40-AP8. (For interpretation of the references to color in this figure legend, the reader is referred to the web version of this article.)

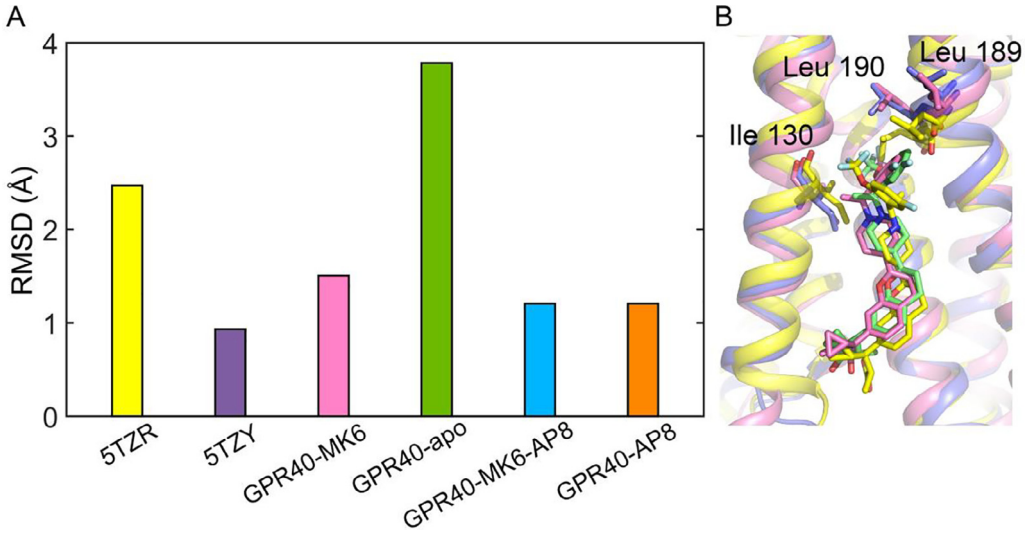

Fig. 8. A. The RMSDs of the best redocked binding poses of AP8 by referencing natural binding mode for each system (yellow: 5TZR; purple: 5TZY; pink: GPR40-MK6; green: GPR40-apo; blue: GPR40-MK6-AP8; orange: GPR40-AP8). B. The redocked binding mode of AP8 in 5TZR and GPR40-MK6 by superimposing with 5TZY. (For interpretation of the references to color in this figure legend, the reader is referred to the web version of this article.)

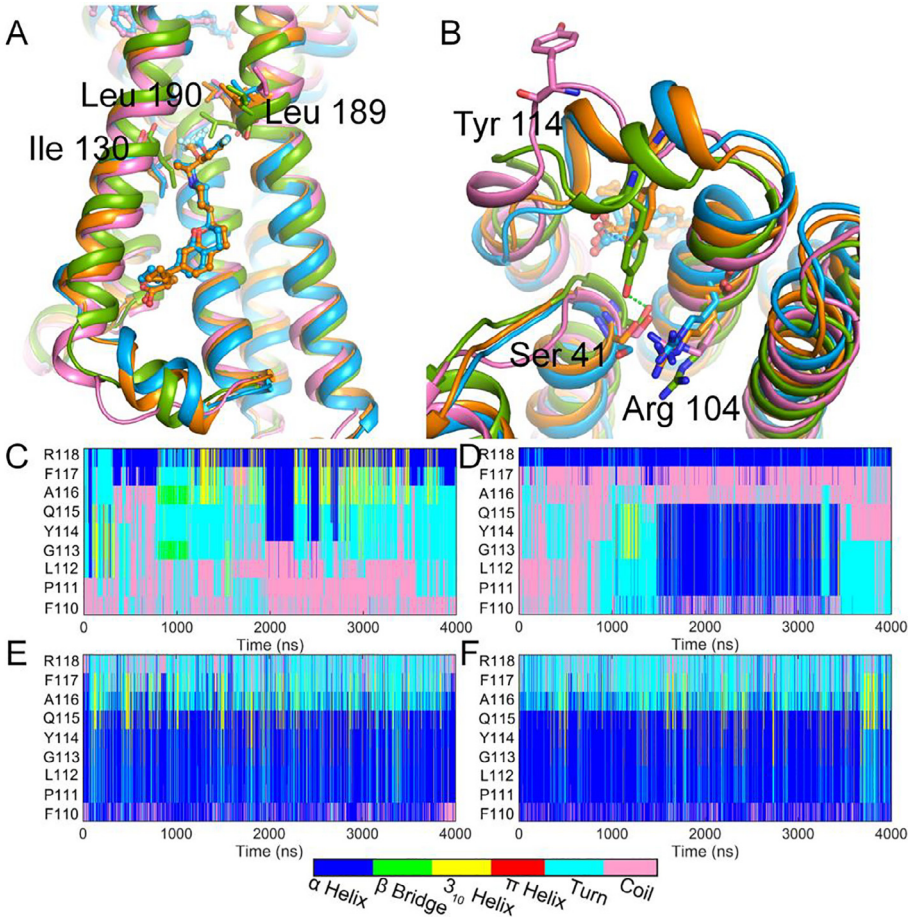

Fig. 9. A, The cartoon schematic diagrams of AP8 binding pocket. B, The conformational states of ICL2 (pink: GPR40-MK6; green: GPR40-apo; blue: GPR40-MK6-AP8; orange: GPR40-AP8). C-F, The monitored secondary structures of ICL2 in GPR40-MK6, GPR40-apo, GPR40-MK6-AP8 and GPR40-AP8, respectively. (For interpretation of the references to color in this figure legend, the reader is referred to the web version of this article.)

(Fig. 9B). In AP8 bound GPR40, ICL2 adopts a short α-helical conformation (Fig. 9B, E and F), Tyr114^{ICL2} forms a hydrogen bond with the carboxylate of AP8 (Fig. 9B and S8A). Lu *et al.* revealed that AP8 binds or unbinds through the ICL2 [27]. And when AP8 enters the binding pocket, ICL2 transforms helical conformation from disordered conformation, and along with Tyr114^{ICL2} turns toward AP8 binding site from outward [27]. Therefore, the conformational dynamics of Tyr114^{ICL2} and ICL2 are crucial for AP8 to entering the pocket. Compared with the partial α-helical conformation of GPR40-apo, the AP8 easily accesses the AgoPAM binding pocket in GPR40-MK6, due to ICL2 being disordered and Tyr114^{ICL2} points outward. The partial α-helical conformation of ICL2 in GPR40-apo closes the lower edge of the site.

3.5. The conformational dynamics of TM4 and TM5 in GPR40-MK6

The conformational differences of TM4 and TM5 that present in GPR40-apo and other systems have been presented in comparison of crystal structures of binary complex and ternary complex [27]. However, the dominant conformation of GPR40-MK6 is more similar to GPR40-AP8 and GPR40-MK6-AP8. Therefore, we compared the representative structures extracted from each cluster by clustering analysis of GPR40-MK6 (Figs. 10, S4 and S9). As shown in Fig. 10A, the TM4 shifts downward (toward the intracellular side), and the TM5 shifts upward (toward the extracellular side). The extracellular end of TM4 shifts toward TM5, and the intracellular half shifts toward the opposite direction. In the late simulation, the TM4 is stabilized in the conformational state that is similar to GPR40-AP8 and GPR40-MK6-AP8 (Fig. 2C and 9A). The significant conformational rearrangement of TM5 and TM4 are associated with remodeling of MK-8666 binding (Fig. 10B). The part that stucked out of the pocket of MK-8666 exhibits various conformational states. On the inside of the pocket, MK-8666 moves deeper into the bottom of the pocket. At the same time, the part sited inside of the pocket slightly moves away from TM4-TM5 (Fig. 10B). As a result, the movement of MK-8666 induces the Leu186$^{5.42}$ to shift upward and closer to the partial agonist binding site (Fig. 10B). And consequently, that brings the TM5 to shift upward. While, in the crystal structure of binary complex, the Leu186$^{5.42}$ is closer to the AgoPAM binding site (Fig. S10).

That is, the change of binding model of MK-8666 induces conformational rearrangement of TM4 and TM5. The downward movement and torsion of TM4 results in the Leu133$^{4.52}$ at the top of AP8 binding site deflecting outward, leaving the top of the AP8 binding site (Fig. 10B and C). The Ile130$^{4.49}$ deflects downward and inward (inside of the helix bundle), leaving the AP8 binding site (Fig. 10C). The Tyr122$^{4.41}$ on the intracellular end of TM4 deflects downward, leaving the bottom of AP8 binding site (Fig. 10D). The upward movement of TM5 results in the Leu189$^{5.45}$ and Leu190$^{5.46}$ moving upward, leaving the top of AP8 binding site (Fig. 10E).

These results reveal that the movements and rotations of TM4 and TM5 make the AgoPAM binding pocket more suitable for accommodating AP8. And the rearrangement of TM5 induced by

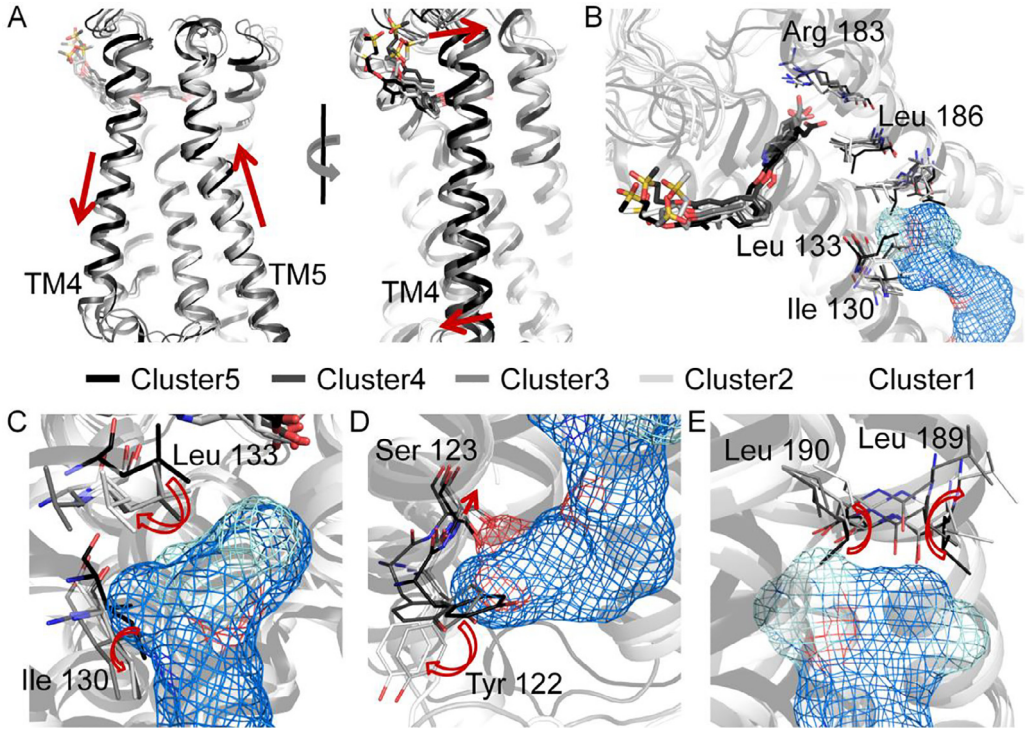

Fig. 10. The conformational dynamics of TM4 and TM5 in GPR40-MK6. A, The movements and torsions of TM4 and TM5. B-E, The conformational rearrangement of residues in AP8 binding site.

MK-8666 indicates that the Leu186$^{5.42}$ plays a crucial role in coordinated coupling between the partial agonist and AgoPAM binding sites. The mutagenesis study for Leu186$^{5.42}$ has highlighted that the residue is essential for receptor activation [58], our results are in line with that. And furthermore, these results also reveal the induced-fit conformational coupling between the partial agonist MK-8666 and AgoPAM binding site.

Additionally, the binding free energy of AP8 in GPR40-MK6-AP8 (-28.86 kcal/mol) is slightly lower than in GPR40-AP8 (-26.61 kcal/mol). Similarly, MK-8666 bound simultaneously can increase the binding affinity of AP8. The hydrophobic residues Gly95, Ala98 and Ala99 on TM3 significantly contribute to the total binding energy in GPR40-MK6-AP8 (Fig. S11). In consequence, the TM3 is important for the positive binding cooperativity between the partial agonist MK-8666 and AgoPAM AP8.

3.6. The cooperativity between partial agonist and AgoPAM binding sites by TM3, TM4 and TM5

The above analysis results reveal that the movement and torsion of TM3, TM4 and TM5 are critical components for cooperativity between partial agonist MK-8666 and AgoPAM AP8 binding sites. Srivastava *et al.* suggested that there is missing the frequently conserved proline at position 4.60 of TM4 in hGPR40, and near the equivalent position there is a glycine residue, Gly139$^{4.58}$. This may impart some degree of flexibility to the extracellular end of TM4, especially in the absence of partial agonist [26]. Consistently, our results reveal that in GPR40-apo, the extracellular end of TM4 is more flexible and shifts toward TM3 in GPR40-apo (Fig. 3A, D and 11A). However, AP8 binding can significantly stabilize TM4 (Fig. 3A, F and 11A).

In addition, transmembrane prolines have already been established that they play significant functional roles in GPCRs [59–64]. The prolines on TM5 (Pro$^{5.50}$) and TM6 (Pro$^{6.50}$) are highly conserved residues of their respective helix among class A GPCRs [65]. In addition, there is proline Pro89$^{3.35}$ near the Phe87$^{3.33}$ and Phe88$^{3.34}$ on TM3. Because of the lack of backbone hydrogen bond donors, proline causes a kink in helix (proline-kink) [66]. The

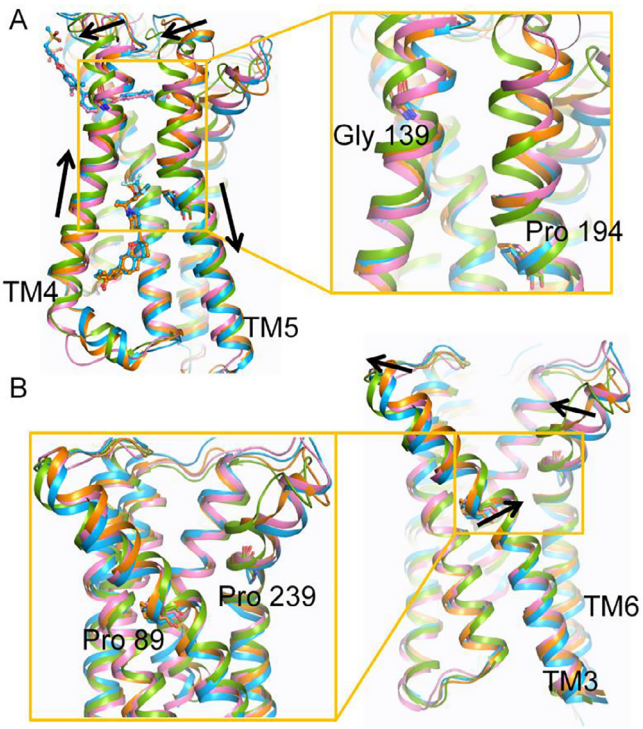

Fig. 11. The conformational differences of TM3, TM4, TM5 and TM6 among the GPR40-MK6 (pink), GPR40-apo (green), GPR40-MK6-AP8 (blue) and GPR40-AP8 (orange). (For interpretation of the references to color in this figure legend, the reader is referred to the web version of this article.)

proline-kink introduces flexibility into TM3, TM5 and TM6, and allows the TM3, TM5 and TM6 to twist and bend. As shown in Fig. 11B, in GPR40-apo compared to other systems, the extracellular end of TM3 shifts toward TM2, the intracellular end of TM3 shifts toward TM5, the middle part (Phe87-Gly95) of TM3 presents a bulge. The bulge is associated with deflections of side chains of Phe87$^{3.33}$ and Phe88$^{3.34}$ (Fig. 5). The extracellular end of TM5 shifts toward TM4, and the intracellular end of TM5 shifts toward TM6 in GPR40-apo compared with other systems (Fig. 11A). In comparison, the conformations of TM3, TM4, TM5 and TM6 are almost similar in GPR40-MK6, GPR40-AP8 and GPR40-MK6-AP8. Therefore, either partial agonist MK-8666 binding or AgoPAM AP8 binding or combination of them can stabilize these transmembrane helices in a similar conformational state.

The inherent structural characteristics of these transmembrane helices give themselves flexibility, and the movements and rotations of these helices couple the two sites. Compared with other systems, the movements and rotations of TM3 and TM4 in GPR40-apo make the side chain of Leu135$^{4.54}$ deflects outward helical bundle, the side chain of Leu138$^{4.57}$ deflects toward TM5, which make free space for the deflections of side chains of Phe87$^{3.33}$ and Phe88$^{3.34}$ (Fig. 12). As a result, the entrance of the partial agonist binding pocket is blocked (Fig. 5B). On the inside of the pocket of GPR40-apo, the movement of TM3 brings the Leu90$^{3.36}$ to deflect toward TM6, and the side chain of Tyr240$^{6.51}$ deflects and stretches into the space of the corresponding Leu90$^{3.36}$ (Fig. 12). TM5 rotates and moves downward in GPR40-apo compared with other systems (Fig. 11A). Accordingly, downward movement of Leu186$^{5.42}$ makes free space for the side chain of Leu138$^{4.57}$ deflecting (Fig. 12).

We carried out the dynamical network analysis and identified the optimal path between MK-8666 and AP8 binding sites by selecting the different combinations of residues as the source and sink nodes (Figs. S12-15). These residues are important for ligands binding (Fig. 4C and S11). The optimal path comprise different residues in the pathway among the four systems. Although the optimal paths are different, each optimal path of ligand-bound GPR40 connects the allosteric communication between the two sites by the intersection of TM3, TM4 and TM5.

In summary, these results indicate that the intersection of TM3, TM4 and TM5 is a key in coordinating the two sites. Upon alternative ligand binding, the bound ligand induces residues of the corresponding site to rearrange. And then, that leads to movements and rotations of TM3, TM4, TM5 and TM6. Accordingly, the conformational states of residues in other sites rearrange. Furthermore, the Leu138$^{4.57}$, Leu186$^{5.42}$ and Leu190$^{5.46}$ coordinate the rearrangement of residues in the two sites (Figs. 11 and 12).

4. Conclusions

In the present work, we revealed the bidirectional induced-fit conformational coupling between the two sites at atomic level. Moreover, we have clarified the mechanism of positive cooperativity between the partial agonist and AgoPAM binding sites. The AgoPAM AP8 bound stabilizes the MK-8666 interacting with GPR40 and increases the binding affinity of MK-8666 (Figs. 3 and 4,

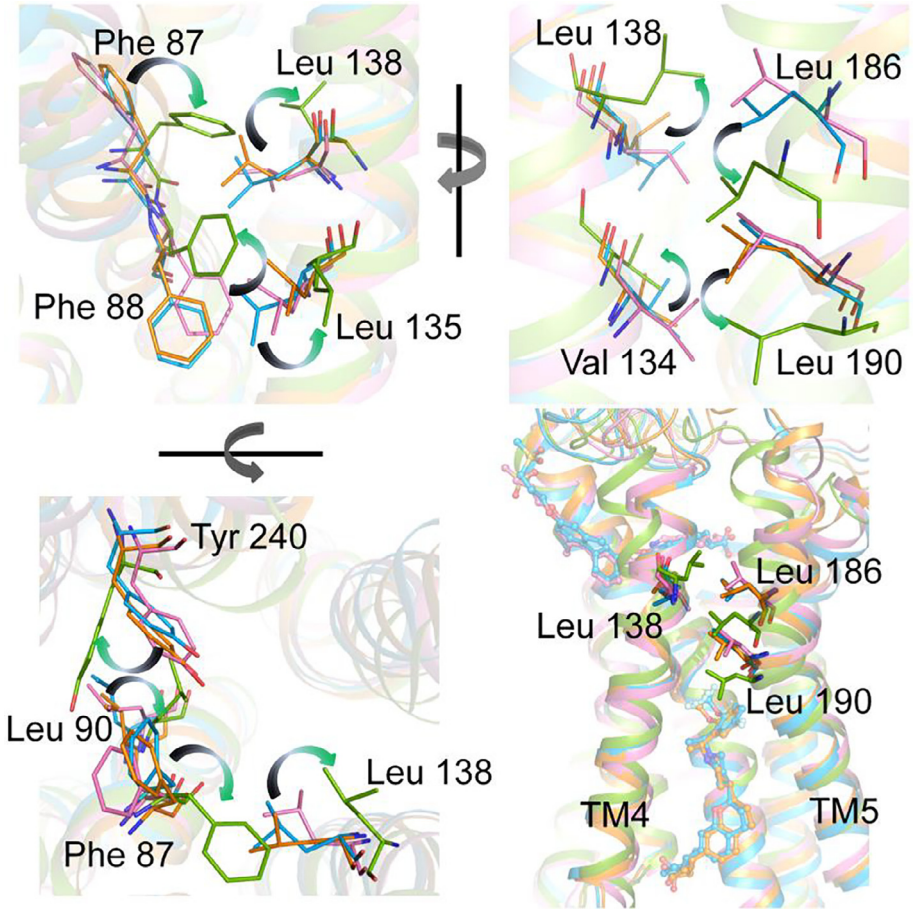

Fig. 12. The critical residues in coordinating the conformational rearrangement of the two sites (GPR40-MK6: pink; GPR40-apo: green; GPR40-MK6-AP8: blue; GPR40-AP8: orange). (For interpretation of the references to color in this figure legend, the reader is referred to the web version of this article.)

Table 1). And additionally, the interhelical space entrance between TM3 and TM4 is maintained in a conformational state where MK-8666 can bind (Fig. 5). Upon MK-8666 binding, the AgoPAM AP8 binding pocket is maintained a similar topological structure of accommodating AP8 as in AP8 bound GPR40 (Figs. 7 and 8).

Because of the presence of Gly139$^{4.58}$ on TM4 and prolines on TM3, TM5 and TM6, which gives inherent flexibility to these helices. Therefore, alternative ligand binding, the conformational changes of residues in the corresponding site induce these helices to movements and rotations. As a result, the perturbed conformations pass to another site through these helices. And residues Ile138$^{4.57}$, Leu186$^{5.42}$ and Leu190$^{5.46}$ between the two sites coordinate the conformational rearrangements of residues in the two sites. The conformational states of TM3, TM4, TM5 and TM6 that make up the two sites are similar among GPR40-MK6, GPR40-AP8 and GPR40-MK6-AP8. That is, either of ligands bound, the other site maintains a conformation state that is similar to ligand bound. The binding of a ligand at one site causes a conformational change at another site, which not only helps to understand the mechanism of cooperativity between the two sites. But also it has potential application value in structure-based drug discovery and design. That can be used for the discovery of new binding sites on protein. This is the starting point of structure-based drug design for the discovery of new framework compounds. It is also valuable to optimize the structures of existing agonists of GPR40 to reduce its side effects based on the conformational changes of the binding site.

CRediT authorship contribution statement

Xiaoli An: Conceptualization, Investigation, Formal analysis, Writing - original draft. **Qifeng Bai:** Conceptualization, Investigation, Validation, Resources. **Zhitong Bing:** Conceptualization, Investigation, Validation, Resources. **Huanxiang Liu:** Supervision, Validation, Writing - review & editing. **Xiaojun Yao:** Supervision, Validation, Writing - review & editing.

Declaration of Competing Interest

The authors declare that they have no known competing financial interests or personal relationships that could have appeared to influence the work reported in this paper.

Acknowledgments

This work was supported by the National Natural Science Foundation of China (Grant No. 21775060). The authors will also wish to thank the supercomputing center of Lanzhou University for providing computational resources.

Appendix A. Supplementary data

Supplementary data to this article can be found online at https://doi.org/10.1016/j.csbj.2021.07.008.

References

[1] Itoh Y, Kawamata Y, Harada M, Kobayashi M, Fujii R, Fukusumi S, et al. Free fatty acids regulate insulin secretion from pancreatic β cells through GPR40. Nature 2003;422(6928):173–6.
[2] Tomita T, Masuzaki H, Iwakura H, Fujikura J, Noguchi M, Tanaka T, et al. Expression of the gene for a membrane-bound fatty acid receptor in the pancreas and islet cell tumours in humans: evidence for GPR40 expression in pancreatic beta cells and implications for insulin secretion. Diabetologia 2006;49(5):962–8.
[3] Briscoe CP, Tadayyon M, Andrews JL, Benson WG, Chambers JK, Eilert MM, et al. The orphan G protein-coupled receptor GPR40 is activated by medium and long chain fatty acids. J Biol Chem 2003;278(13):11303–11.
[4] Kotarsky K, Nilsson N, Flodgren E, Owman C, Olde B. A human cell surface receptor activated by free fatty acids and thiazolidinedione drugs. Biochem Biophys Res Commun 2003;301(2):406–10.
[5] Briscoe CP, Peat AJ, McKeown SC, Corbett DF, Goetz AS, Littleton TR, et al. Pharmacological regulation of insulin secretion in MIN6 cells through the fatty acid receptor GPR40: identification of agonist and antagonist small molecules. Br J Pharmacol 2006;148(5):619–28.
[6] Schnell S, Schaefer M, Schofl C. Free fatty acids increase cytosolic free calcium and stimulate insulin secretion from beta-cells through activation of GPR40. Mol Cell Endocrinol 2007;263(1–2):173–80.
[7] Kebede M, Alquier T, Latour MG, Semache M, Tremblay C, Poitout V. The fatty acid receptor GPR40 plays a role in insulin secretion in vivo after high-fat feeding. Diabetes 2008;57(9):2432–7.
[8] Poitout V, Lin D-H. Modulating GPR40: therapeutic promise and potential in diabetes. Drug Discov Today 2013;18(23-24):1301–8.
[9] Burant CF. Activation of GPR40 as a therapeutic target for the treatment of type 2 diabetes. Diabetes Care 2013;36(Supplement_2):S175–9.
[10] Choi YJ, Shin D, Lee JY. G-protein coupled receptor 40 agonists as novel therapeutics for type 2 diabetes. Arch Pharm Res 2014;37(4):435–9.
[11] Negoro N, Sasaki S, Mikami S, Ito M, Suzuki M, Tsujihata Y, et al. Discovery of TAK-875: A Potent, Selective, and Orally Bioavailable GPR40 Agonist. ACS Med Chem Lett 2010;1(6):290–4.
[12] Brown SP, Dransfield PJ, Vimolratana M, Jiao X, Zhu L, Pattaropong V, et al. Discovery of AM-1638: A Potent and Orally Bioavailable GPR40/FFA1 Full Agonist. ACS Med Chem Lett 2012;3(9):726–30.
[13] Lin D-H, Zhang J, Zhuang R, Li F, Nguyen K, Chen M, et al. AMG 837: a novel GPR40/FFA1 agonist that enhances insulin secretion and lowers glucose levels in rodents. PLoS ONE 2011;6(11):e27270. https://doi.org/10.1371/journal.pone.002727010.1371/journal.pone.0027270.g00110.1371/journal.pone.0027270.g00210.1371/journal.pone.0027270.g00310.1371/journal.pone.0027270.g00410.1371/journal.pone.0027270.g00510.1371/journal.pone.0027270.t001.
[14] Sasaki S, Kitamura S, Negoro N, Suzuki M, Tsujihata Y, Suzuki N, et al. Design, synthesis, and biological activity of potent and orally available G protein-coupled receptor 40 agonists. J Med Chem 2011;54(5):1365–78.
[15] Christiansen E, Hansen SV, Urban C, Hudson BD, Wargent ET, Grundmann M, et al. Discovery of TUG-770: A Highly Potent Free Fatty Acid Receptor 1 (FFA1/GPR40) Agonist for Treatment of Type 2 Diabetes. ACS Med Chem Lett 2013;4(5):441–5.
[16] Christiansen E, Urban C, Grundmann M, Due-Hansen ME, Hagesaether E, Schmidt J, et al. Identification of a potent and selective free fatty acid receptor 1 (FFA1/GPR40) agonist with favorable physicochemical and in vitro ADME properties. J Med Chem 2011;54(19):6691–703.
[17] Hara T, Hirasawa A, Sun Q, Sadakane K, Itsubo C, Iga T, et al. Novel selective ligands for free fatty acid receptors GPR120 and GPR40. Naunyn-Schmiedeberg's Arch Pharmacol 2009;380(3):247–55.
[18] Zhou C, Tang C, Chang E, Ge M, Lin S, Cline E, et al. Discovery of 5-aryloxy-2,4-thiazolidinediones as potent GPR40 agonists. Bioorg Med Chem Lett 2010;20(3):1298–301.
[19] Walsh SP, Severino A, Zhou C, He J, Liang GB, Tan CP, et al. 3-Substituted 3-(4-aryloxyaryl)-propanoic acids as GPR40 agonists. Bioorg Med Chem Lett 2011;21(11):3390–4.
[20] Sunil V, Verma MK, Oommen AM, Sadasivuni M, Singh J, Vijayraghav DN, et al. CNX-011-67, a novel GPR40 agonist, enhances glucose responsiveness, insulin secretion and islet insulin content in n-STZ rats and in islets from type 2 diabetic patients. *BMC*. Pharmacol Toxicol 2014;15(1). https://doi.org/10.1186/2050-6511-15-19.
[21] Leifke E, Naik H, Wu J, Viswanathan P, Demanno D, Kipnes M, et al. A multiple-ascending-dose study to evaluate safety, pharmacokinetics, and pharmacodynamics of a novel GPR40 agonist, TAK-875, in subjects with type 2 diabetes. Clin Pharmacol Ther 2012;92(1):29–39.
[22] Naik H, Vakilynejad M, Wu J, Viswanathan P, Dote N, Higuchi T, et al. Safety, tolerability, pharmacokinetics, and pharmacodynamic properties of the GPR40 agonist TAK-875: results from a double-blind, placebo-controlled single oral dose rising study in healthy volunteers. J Clin Pharmacol 2012;52(7):1007–16.
[23] Kaku K, Enya K, Nakaya R, Ohira T, Matsuno R. Efficacy and safety of fasiglifam (TAK-875), a G protein-coupled receptor 40 agonist, in Japanese patients with type 2 diabetes inadequately controlled by diet and exercise: a randomized, double-blind, placebo-controlled, phase III trial. Diabetes Obes Metab 2015;17(7):675–81.
[24] Li X, Zhong K, Guo Z, Zhong D, Chen X. Fasiglifam (TAK-875) Inhibits Hepatobiliary Transporters: A Possible Factor Contributing to Fasiglifam-Induced Liver Injury. Drug Metab Dispos 2015;43(11):1751–9.
[25] Lin DC, Guo Q, Luo J, Zhang J, Nguyen K, Chen M, et al. Identification and pharmacological characterization of multiple allosteric binding sites on the free fatty acid 1 receptor. Mol Pharmacol 2012;82(5):843–59.

[26] Srivastava A, Yano J, Hirozane Y, Kefala G, Gruswitz F, Snell G, et al. High-resolution structure of the human GPR40 receptor bound to allosteric agonist TAK-875. Nature 2014;513(7516):124–7.
[27] Lu J, Byrne N, Wang J, Bricogne G, Brown FK, Chobanian HR, et al. Structural basis for the cooperative allosteric activation of the free fatty acid receptor GPR40. Nat Struct Mol Biol 2017;24(7):570–7.
[28] Hamelberg D, Mongan J, McCammon JA. Accelerated molecular dynamics: a promising and efficient simulation method for biomolecules. J Chem Phys 2004;120(24):11919–29.
[29] Miao Y, Feher VA, McCammon JA. Gaussian Accelerated Molecular Dynamics: Unconstrained Enhanced Sampling and Free Energy Calculation. J Chem Theory Comput 2015;11(8):3584–95.
[30] Torrie GM, Valleau JP. Nonphysical Sampling Distributions in Monte Carlo Free-Energy Estimation: Umbrella Sampling. J Comput Phys 1977;23(2):187–99.
[31] Isralewitz B, Gao M, Schulten K. Steered molecular dynamics and mechanical functions of proteins. Curr Opin Struct Biol 2001;11(2):224–30.
[32] Laio A, Parrinello M. Escaping free-energy minima. PNAS 2002;99(20):12562–6.
[33] Babin V, Roland C, Sagui C. Adaptively biased molecular dynamics for free energy calculations. J Chem Phys 2008;128(13):134101.
[34] Miao Y, McCammon JA. Graded activation and free energy landscapes of a muscarinic G-protein–coupled receptor. PNAS 2016;113(43):12162–7.
[35] Wang YT, Chan YH. Understanding the molecular basis of agonist/antagonist mechanism of human mu opioid receptor through gaussian accelerated molecular dynamics method. Sci Rep 2017;7(1):7828.
[36] Miao Y, Bhattarai A, Nguyen ATN, Christopoulos A, May LT. Structural Basis for Binding of Allosteric Drug Leads in the Adenosine A1 Receptor. Sci Rep 2018;8(1):16836.
[37] Miao Y, McCammon JA. Mechanism of the G-protein mimetic nanobody binding to a muscarinic G-protein-coupled receptor. PNAS 2018;3036–3041(115):12.
[38] Bhattarai A, Miao Y. Gaussian accelerated molecular dynamics for elucidation of drug pathways. Expert Opin Drug Discov 2018;13(11):1055–65.
[39] Wang J, Miao Y. Mechanistic Insights into Specific G Protein Interactions with Adenosine Receptors. J Phys Chem B 2019;123(30):6462–73.
[40] Bhattarai A, Wang J, Miao Y. G-Protein-Coupled Receptor-Membrane Interactions Depend on the Receptor Activation State. J Comput Chem 2020;41(5):460–71.
[41] Kuhn B, Kollman PA. Binding of a Diverse Set of Ligands to Avidin and Streptavidin: An Accurate Quantitative Prediction of Their Relative Affinities by a Combination of Molecular Mechanics and Continuum Solvent Models. J Med Chem 2000;43:3786–91.
[42] Sastry GM, Adzhigirey M, Day T, Annabhimoju R, Sherman W. Protein and ligand preparation: parameters, protocols, and influence on virtual screening enrichments. J Comput Aided Mol Des 2013;27(3):221–34.
[43] Pandy-Szekeres G, Munk C, Tsonkov TM, Mordalski S, Harpsoe K, Hauser AS, et al. GPCRdb in 2018: adding GPCR structure models and ligands. Nucleic Acids Res 2018;46(D1):D440–6.
[44] Cheng RKY, Fiez-Vandal C, Schlenker O, Edman K, Aggeler B, Brown DG, et al. Structural insight into allosteric modulation of protease-activated receptor 2. Nature 2017;545(7652):112–5.
[45] Jo S, Kim T, Iyer VG, Im W. Software News and Updates CHARMM-GUI: A Web-Based Graphical User Interface for CHARMM. J Comput Chem 2008;29(11):1859–65.
[46] Brooks BR, Brooks 3rd CL, Mackerell Jr AD, Nilsson L, Petrella RJ, Roux B, Won Y, Archontis G, Bartels C, Boresch S, Caflisch A, Caves L, Cui Q, Dinner AR, Feig M, Fischer S, Gao J, Hodoscek M, Im W, Kuczera K, Lazaridis T, Ma J, Ovchinnikov V, Paci E, Pastor RW, Post CB, Pu JZ, Schaefer M, Tidor B, Venable RM, Woodcock HL, Wu X, Yang W, York DM, Karplus M. CHARMM: the biomolecular simulation program. J Comput Chem 2009;30(10):1545–614.
[47] Lee J, Cheng X, Swails JM, Yeom MS, Eastman PK, Lemkul JA, et al. CHARMM-GUI Input Generator for NAMD, GROMACS, AMBER, OpenMM, and CHARMM/OpenMM Simulations Using the CHARMM36 Additive Force Field. J Chem Theory Comput 2016;12(1):405–13.
[48] Lomize MA, Pogozheva ID, Joo H, Mosberg HI, Lomize AL. OPM database and PPM web server: resources for positioning of proteins in membranes. Nucleic Acids Res 2012;40(Database issue):D370–6.
[49] Jorgensen WL, Chandrasekhar J, Madura JD, Impey RW, Klein ML. Comparison of simple potential functions for simulating liquid water. J Chem Phys 1983;79(2):926–35.
[50] Maier JA, Martinez C, Kasavajhala K, Wickstrom L, Hauser KE, Simmerling C. ff14SB: Improving the Accuracy of Protein Side Chain and Backbone Parameters from ff99SB. J Chem Theory Comput 2015;11(8):3696–713.
[51] Wang JM, Wolf RM, Caldwell JW, Kollman PA, Case DA. Development and Testing of a General Amber Force Field. J Comput Chem 2004;25(9):1157–74.
[52] Skjevik Åge A, Madej Benjamin D, Walker Ross C, Teigen Knut. LIPID11: a modular framework for lipid simulations using amber. J Phys Chem B 2012;116(36):11124–36.
[53] Frisch, M. J.; Trucks, G. W.; Schlegel, H. B.; Scuseria, G. E.; Robb, M. A.; Cheeseman, J. R.; Montgomery, J., J. A.; Vreven, T.; Kudin, K. N.; Burant, J. C.; Millam, J. M.; Iyengar, S. S.; Tomasi, J.; Barone, V.; Mennucci, B.; Cossi, M.; Scalmani, G.; Rega, N.; Petersson, G. A.; Nakatsuji, H.; Hada, M.; Ehara, M.; Toyota, K.; Fukuda, R.; Hasegawa, J.; Ishida, M.; Nakajima, T.; Honda, Y.; Kitao, O.; Nakai, H.; Klene, M.; Li, X.; Knox, J. E.; Hratchian, H. P.; Cross, J. B.; Bakken, V.; Adamo, C.; Jaramillo, J.; Gomperts, R.; Stratmann, R. E.; Yazyev, O.; Austin, A. J.; Cammi, R.; Pomelli, C.; Ochterski, J. W.; Ayala, P. Y.; Morokuma, K.; Voth, G. A.; Salvador, P.; Dannenberg, J. J.; Zakrzewski, V. G.; Dapprich, S.; Daniels, A. D.; Strain, M. C.; Farkas, O.; Malick, D. K.; Rabuck, A. D.; Raghavachari, K.; Foresman, J. B.; Ortiz, J. V.; Cui, Q.; Baboul, A. G.; Clifford, S.; Cioslowski, J.; Stefanov, B. B.; Liu, G.; Liashenko, A.; Piskorz, P.; Komaromi, I.; Martin, R. L.; Fox, D. J.; Keith, T.; Al-Laham, M. A.; Peng, C. Y.; Nanayakkara, A.; Challacombe, M.; Gill, P. M. W.; Johnson, B.; Chen, W.; Wong, M. W.; Gonzalez, C.; Pople, J. A., Gaussian 09, Gaussian, Inc. Wallingford, CT, USA 2009.
[54] Fox Thomas, Kollman Peter A. Application of the RESP Methodology in the Parametrization of Organic Solvents. J Phys Chem B 1998;102(41):8070–9.
[55] Darden T, York D, Pedersen L. Particle mesh Ewald: An N·log(N) method for Ewald sums in large systems. J Chem Phys 1993;98(12):10089–92.
[56] Ryckaert JP, Ciccotti G, Berendsen HJC. Numerical integration of the cartesian equations of motion of a system with constraints: molecular dynamics of n-alkanes. J Comput Phys 1977;23(3):327–41.
[57] Friesner RA, Banks JL, Murphy RB, A HT, Klicic JJ, Mainz DTR, M P, Knoll EH, Shelley M, Perry JK, Shaw DE, Francis P, Shenkin PS. Glide: A New Approach for Rapid, Accurate Docking and Scoring. 1. Method and Assessment of Docking Accuracy. J Med Chem 2004;47(7):1739–49.
[58] Tikhonova IG, Poerio E. Free fatty acid receptors: structural models and elucidation of ligand binding interactions. BMC Struct Biol 2015;15:16.
[59] Wess J, Nanavati S, Vogel Z, Maggio R. Functional role of proline and tryptophan residues highly conserved among G protein-coupled receptors studied by mutational analysis of the m3 muscarinic receptor. EMBO J 1993;12(1):331–8.
[60] Hong S, Ryu KS, Oh MS, Ji I, Ji TH. Roles of Transmembrane Prolines and Proline-induced Kinks of the Lutropin/Choriogonadotropin Receptor*. J Biol Chem 1997;272(7):4166–71.
[61] Stitham J, Martin KA, Hwa J. The Critical Role of Transmembrane Prolines in Human Prostacyclin Receptor Activation. Mol Pharmacol 2002;61(5):1202–10.
[62] Haffemayer B, Richard E, Mattras H, Marie J. Functional role of the conserved proline in helix 6 of the human bradykinin B2 receptor. Biochem Biophys Res Commun 2008;366(4):1001–6.
[63] Mazna P, Grycova L, Balik A, Zemkova H, Friedlova E, Obsilova V, et al. The role of proline residues in the structure and function of human MT2 melatonin receptor. J Pineal Res 2008;45(4):361–72.
[64] Van Arnam EB, Lester HA, Dougherty DA. Dissecting the functions of conserved prolines within transmembrane helices of the D2 dopamine receptor. ACS Chem Biol 2011;6(10):1063–8.
[65] Ballesteros JA, Weinstein H. Integrated methods for the construction of three-dimensional models and computational probing of structure-function relations in G protein-coupled receptors. Methods Neurosci 1995;25:366–428.
[66] von Heijne G. Proline Kinks in Transmembrane α-Helices. J Mol Biol 1991;218(3):499–503.